Front. Mech. Eng. 2023, 18(2): 23
https://doi.org/10.1007/s11465-022-0739-6

RESEARCH ARTICLE

Design and modeling of continuum robot based on virtual-center of motion mechanism

Guoxin LI[a], Jingjun YU[a], Yichao TANG[b], Jie PAN[a], Shengge CAO[a], Xu PEI (✉)[a]

[a] *School of Mechanical Engineering and Automation, Beihang University, Beijing 100191, China*
[b] *Beijing Special Engineering Design and Research Institute, Beijing 100143, China*

✉ *Corresponding author. E-mail: goingxu@163.com (Xu PEI)*

ABSTRACT Continuum robot has attracted extensive attention since its emergence. It has multi-degree of freedom and high compliance, which give it significant advantages when traveling and operating in narrow spaces. The flexural virtual-center of motion (VCM) mechanism can be machined integrally, and this way eliminates the assembly between joints. Thus, it is well suited for use as a continuum robot joint. Therefore, a design method for continuum robots based on the VCM mechanism is proposed in this study. First, a novel VCM mechanism is formed using a double leaf-type isosceles-trapezoidal flexural pivot (D-LITFP), which is composed of a series of superimposed LITFPs, to enlarge its stroke. Then, the pseudo-rigid body (PRB) model of the leaf is extended to the VCM mechanism, and the stiffness and stroke of the D-LITFP are modeled. Second, the VCM mechanism is combined to form a flexural joint suitable for the continuum robot. Finally, experiments and simulations are used to validate the accuracy and validity of the PRB model by analyzing the performance (stiffness and stroke) of the VCM mechanism. Furthermore, the motion performance of the designed continuum robot is evaluated. Results show that the maximum stroke of the VCM mechanism is approximately 14.2°, the axial compressive strength is approximately 1915 N/mm, and the repeatable positioning accuracies of the continuum robot is approximately ±1.47° (bending angle) and ±2.46° (bending direction).

KEYWORDS VCM mechanism, continuum robot, flexural joint, pseudo-rigid body model, cable-driven

1 Introduction

Continuum robots, also known as snake-arm or elephant-trunk robots, have become popular in the last 30 years. They have flexible and hyper-redundant structures. One of their main advantages over conventional rigid robots is the ability to travel in narrow, confined areas and reach specific locations without damaging themselves or the environment. This feature allows robots to interact with people and other objects more safely. Many researchers focus on the development of continuum robots for applications in narrow spaces due to their advantages, such as minimally invasive surgery [1–3], aviation inspection and repair [4,5], nuclear power [6,7], in-space inspection [8], submarine pipeline inspection [9], and other fields [10,11]. Continuum robots can be categorized into two according to the type of backbone: rigid backbone and flexible backbone. The connecting links of a rigid backbone continuum robot are connected using rotation pairs (R pairs) [12], Hooke hinges (U pair) [13], and spherical hinges (S pair) [14]. This type of continuum robot has distinct links and joints. However, it still has the characteristics of a continuum robot due to the sufficient number of joints, and its control is also inclined to active control, with 3 or 4 cables per joint for control. Among the rigid backbone continuum robots, several continuum robots from OC Robotics are the most successful cases [15]. Rigid continuum robots designed with rolling joints as the backbone are also a major research topic [16]. The other is the flexural backbone continuum robot, which has a body structure that is composed of flexural joints or soft materials, such as springs [17,18], pneumatic artificial muscles [19], hyper-elastic nitinol rods with base plates [20,21], flexural mechanisms [22–24], and concentric tube structures [25,26]. Obviously, this type of continuum robot is more in line with the concept of the continuous manipulator and can produce a continuous bending deformation effect. The origami mechanism also extends a new direction for the structural design of flexural continuum robots [27–29]. However, some

Received May 10, 2022; accepted September 7, 2022

research has been conducted on variable-length continuum robots recently [30–32], which not only enhances the functionality of continuum robots but also breaks the bottleneck of conventional continuum robots in terms of length.

Continuum robots with flexure mechanisms as their backbone utilize their structures to achieve bending. However, flexure mechanisms, mainly including notch-type and leaf-type [33,34], generally have smaller bending angles and require longer arms and more joints for the same stroke due to the limitations of their structures. This condition is a great challenge for accurate modeling and control of continuum robots. This aspect has also attracted the attention of scholars on large-stroke flexural pivots, such as combining notched-type and leaf-type pivots into different forms of Hooke hinge as joints [35–37], which are mostly used in continuum robots for minimally invasive surgery. Another type of continuum robot, which takes the whole hyper-elastic nitinol tube as the backbone, uses laser cutting to process a series of flexural mechanisms on the tube wall for realizing the motion of the continuum robot without assembly [38,39], which obscures the concept of movement joint to some extent.

On the basis of the abovementioned discussion, the virtual-center of motion (VCM) mechanism is designed as the main configuration of the continuum robot, and its advantages of integrated processing can be introduced into the design and manufacturing of the continuum robot. This approach can improve the motion accuracy of the continuum robot. Furthermore, the VCM mechanism utilizes double leaf-type isosceles-trapezoidal flexural pivot (D-LITFP) to enlarge stroke, and the D-LITFP is configured in parallel to improve its stiffness. Then, the VCM mechanism and the continuum robot composed of VCM mechanisms are modeled. Finally, the modeling and performance of the VCM mechanism and the continuum robot are validated by experiments and simulations.

2 Design and modeling

Compared with rigid hinges such as spherical and Hooke hinges, the main advantage of the VCM mechanism is that it can be processed integrally and generally does not require assembly. Thus, it reduces the assembly tolerance brought by rigid hinges and precision design requirements. At the same time, the stiffness of the VCM mechanism can ensure the continuity and uniform distribution of bending action. This feature provides the feasibility of the VCM mechanism for the design of continuum robots. The main problem for the flexural VCM mechanism is the restriction of its rotation stroke. Thus, a flexural VCM mechanism suitable for the flexural joint of continuum robots is designed in this study, which utilizes D-LITFP to enlarge its stroke. Then, the pseudo-rigid body (PRB) model of the leaf is extended to the VCM mechanism, and its stiffness and stroke are modeled accurately.

2.1 Design of VCM mechanism

The proposed VCM mechanism is composed of two identical large-stroke D-LITFPs in parallel, as shown in Fig. 1(a). The D-LITFP is superposed by two LITFPs in series to obtain a large stroke. The instantaneous center of rotation (ICR) of the two LITFPs are at the same point O on the lower surface (Fig. 1(b)). The ICRs of two parallel flexible D-LITFPs form the rotation axis of the VCM mechanism. The D-LITFP is also designed as a tensioned structure to withstand higher loads (a tensioned leaf is more stable than a compressed leaf for the same parameters). Overall, the VCM mechanism can rotate around the instantaneous axis of rotation (the line of the ICRs), which has 1 degree of freedom.

2.2 PRB model for the LITFP

For the VCM mechanism that can be used as the flexural joint, the stroke θ, stiffness, and axial compressive strength are critical. First, a single LITFP is modeled and analyzed based on the PRB model.

The main parameters of an LITFP include H, h_f, and φ, and its ICR is at the intersection of the extension lines of two leaves AD and BC (Fig. 2(a)). Where h_f and H are the vertical coordinates of the endpoints of the flexible leaf BC in the coordinate system $\{XOY\}$, and a_1 and a_2 are the horizontal coordinates. φ is the angle between the leaf and the Y-axis. To represent the position of the ICR, the

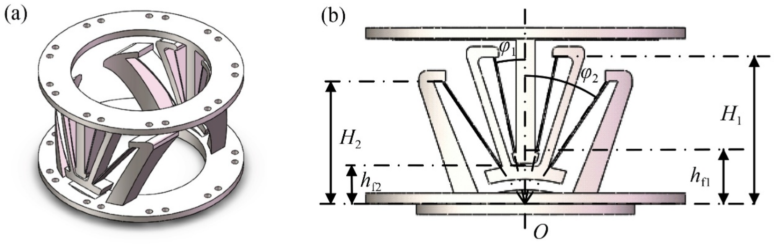

Fig. 1 Design of the virtual-center of motion mechanism: (a) structure of the virtual-center of motion mechanism and (b) structural parameters of the double leaf-type isosceles-trapezoidal flexural pivot.

coefficient n is introduced to represent it. Their parametric relationship can be expressed as

$$n = \frac{H}{H - h_\mathrm{f}},\ n \in [1, +\infty), \tag{1}$$

$$\begin{cases} a_1 = h_\mathrm{f} \tan\varphi, \\ a_2 = H \tan\varphi. \end{cases} \tag{2}$$

When the LITFP is subjected to a pure bending moment M, its deformation is shown in Fig. 2(b). Figure 2(c) is the force analysis diagram of link DC. The corresponding relationships are as follows:

$$\begin{cases} F_{Cx} = F_\mathrm{NC} \sin(\varphi + \alpha_1) - F_\mathrm{RC} \cos(\varphi + \alpha_1), \\ F_{Cy} = F_\mathrm{NC} \cos(\varphi + \alpha_1) + F_\mathrm{RC} \sin(\varphi + \alpha_1), \\ F_{Dx} = F_\mathrm{ND} \sin(\varphi - \alpha_2) - F_{\mathrm{R}D} \cos(\varphi - \alpha_2), \\ F_{Dy} = -F_\mathrm{ND} \cos(\varphi - \alpha_2) - F_\mathrm{RD} \sin(\varphi - \alpha_2), \end{cases} \tag{3}$$

where $F_{\mathrm{R}C}$ and $F_{\mathrm{R}D}$ are the radial forces exerted by link BC and AD on points C and D of link DC, which are perpendicular to the links BC and AD, respectively, and F_NC and F_ND are the axial forces applied to link DC, which are parallel to links BC and AD, respectively. While F_{Cx}, F_{Cy}, F_{Dx}, and F_{Dy} are the x and y components of the forces on points C and D of link CD, respectively, and α_1 and α_2 are bending angles of link BC and AD under the action of bending moment M, respectively (Fig. 2(d)), which can be given by

$$\begin{cases} \alpha_1 = 2\arcsin\dfrac{\overline{CC'}}{2l_\mathrm{r}}, \\ \alpha_2 = 2\arcsin\dfrac{\overline{DD'}}{2l_\mathrm{r}}, \end{cases} \tag{4}$$

where l_r is the length of the rigid link $A'D$ and $B'C$ of the PRB model. $\overline{CC'}$ and $\overline{DD'}$ are the displacements of points C and D, respectively, and their solving process can be referred to Ref. [40].

The radial forces F_RC and F_RD can be calculated as

$$\begin{cases} F_\mathrm{RC} = \dfrac{K_{BC}\alpha_1}{l_\mathrm{r}}, \\ F_\mathrm{RD} = \dfrac{K_{AD}\alpha_2}{l_\mathrm{r}}, \end{cases} \tag{5}$$

where K_{BC} and K_{AD} are the bending stiffness of links BC

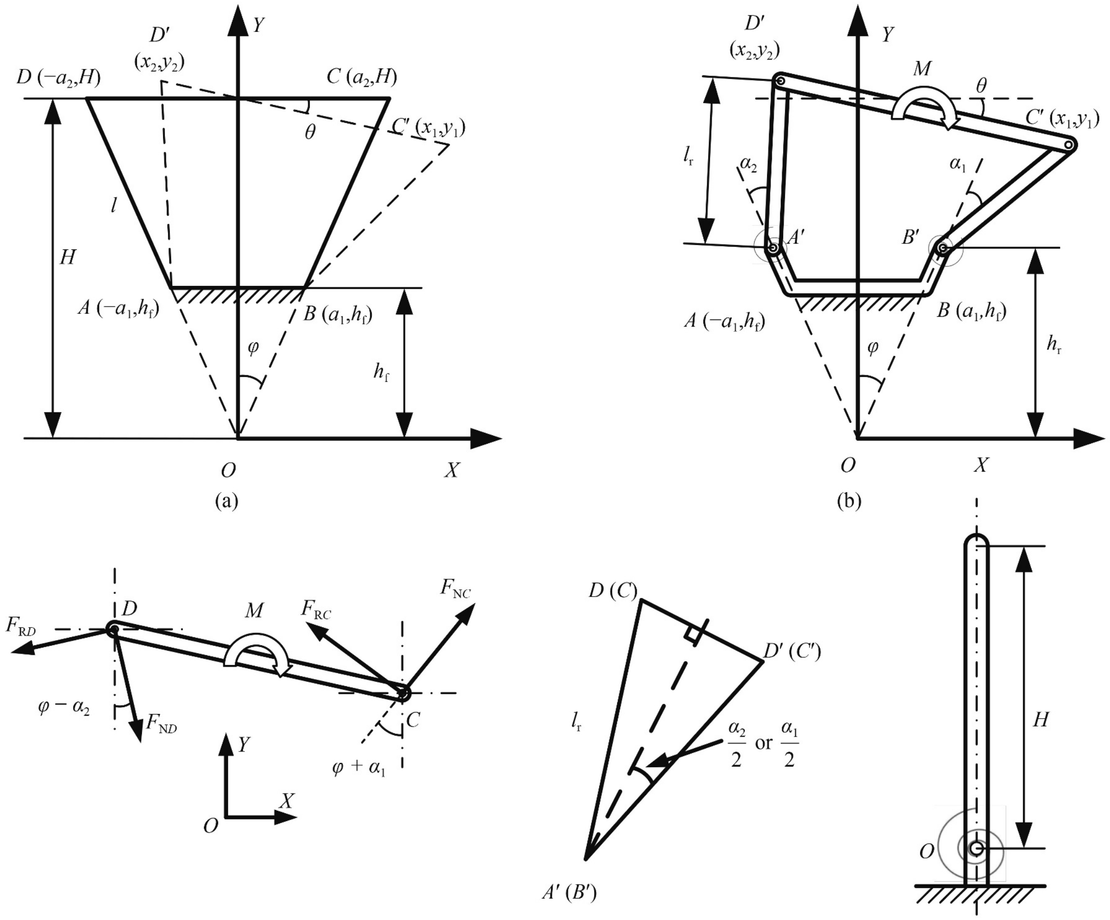

(a) (b) (c) (d) (e)

Fig. 2 Pseudo-rigid body model of a leaf-type isosceles-trapezoidal flexural pivot (LITFP): (a) analytic model of an LITFP, (b) equivalent four-bar model of an LITFP, (c) force analysis of the link DC, (d) bending angle at point D or C, and (e) equivalent pin-joint model of an LITFP.

and AD, respectively, which can also be calculated according to our previous research [40].

The equation for the moment balance on the link DC satisfies

$$\begin{cases} F_{Cx}+F_{Dx}=0, \\ F_{Cy}+F_{Dy}=0, \\ 2bF_{Dx}\sin\theta+2bF_{Dy}\cos\theta=M. \end{cases} \tag{6}$$

By combining Eqs. (2)–(6), the bending moment M can be obtained:

$$M=2b\frac{F_{\mathrm{RC}}\cos(\varphi-\alpha_2+\theta)+F_{\mathrm{R}D}\cos(\varphi+\alpha_1-\theta)}{\sin(2\varphi+\alpha_1-\alpha_2)}. \tag{7}$$

When the bending angle θ is small, it can be obtained by Taylor's expansion of trigonometric functions.

$$\begin{cases} \sin\theta=\theta, \\ \cos\theta=1. \end{cases} \tag{8}$$

Substituting Eq. (8) into Eq. (7) yields

$$M=\frac{8EI(H^2+Hh_{\mathrm{f}}+h_{\mathrm{f}}^2)\cos\varphi}{(H-h_{\mathrm{f}})^3}\cos\left(\frac{H+8h_{\mathrm{f}}}{8(H-h_{\mathrm{f}})}\right)\theta, \tag{9}$$

where E and I are the elastic modulus and moment of inertia of the leaf, respectively.

In this case, the stiffness K of the equivalent single pin-joint model shown in Fig. 2(e) is

$$K=\frac{8EI(H^2+Hh_{\mathrm{f}}+h_{\mathrm{f}}^2)\cos\varphi}{(H-h_{\mathrm{f}})^3}\cos\frac{H+8h_{\mathrm{f}}}{8(H-h_{\mathrm{f}})}. \tag{10}$$

In particular, when $h_{\mathrm{f}}/H\leqslant 6/17$, we have $(H+8h_{\mathrm{f}})/[8(H-h_{\mathrm{f}})]\leqslant 1$. In this case,

$$\cos\frac{H+8h_{\mathrm{f}}}{8(H-h_{\mathrm{f}})}\approx 1. \tag{11}$$

Then, the stiffness of the equivalent single pin-joint model can be further simplified to

$$K=\frac{8EI(H^2+Hh_{\mathrm{f}}+h_{\mathrm{f}}^2)\cos\varphi}{(H-h_f)^3}. \tag{12}$$

Substituting Eq. (1) into Eq. (12) yields

$$K=\frac{8nEI(3n^2-3n+1)\cos\varphi}{H}. \tag{13}$$

In the PRB model analysis of the leaf [40], when the rotational angle reaches the maximum $\theta_{\max}$, the bending moment of the leaf is also the maximum, so the maximum bending moment $M_{\max}$ received by the leaf is

$$M_{\max}=\frac{2EI(3n-1)\cos\varphi}{H}\theta_{\max}. \tag{14}$$

Then, the maximum stress $\sigma_{\max}$ received by the leaf on LITFP is

$$\sigma_{\max}=\frac{M_{\max}t}{2I}=\frac{Et(3n-1)n\cos\varphi}{H}\theta_{\max}, \tag{15}$$

where t is the thickness of the leaf.

When the maximum stress on the leaf reaches the yield strength (S_{y}), LITFP has the maximum rotational angle $\theta_{\max}$ (stroke):

$$\theta_{\max}=\frac{H}{Etn(3n-1)\cos\varphi}S_{\mathrm{y}}. \tag{16}$$

2.3 PRB model for the D-LITFP

The main characteristic of the LITFP is that its ICR is not on the pivot. Thus, the symmetrical or asymmetrical superposition combination can be fully used to adjust the stiffness and expand the stroke for obtaining the VCM mechanism with a large stroke. As shown in Fig. 3(a), two LITFPs are selected and reasonably configured in positions to ensure that their ICRs are overlapped. Then, an intermediate element (IE) to connect the stand (S) of one LITFP is added to the movement element (ME) of the other LITFP, and the remaining S and ME become the S and ME of the D-LITFP.

The PRB model of LITFP in the abovementioned section can be also used for similar modeling and analysis of the D-LITFP. The PRB model is shown in Fig. 3(b). Under the action of a pure bending moment M, LITFP 1 rotates θ_1 relative to LITFP 2, and LITFP 2 rotates θ_2 relative to S. Then, the rotation angle of the whole D-LITFP is θ_{d}, and we have

$$\theta_{\mathrm{d}}=\theta_1+\theta_2, \tag{17}$$

$$M=K_1\theta_1=K_2\theta_2, \tag{18}$$

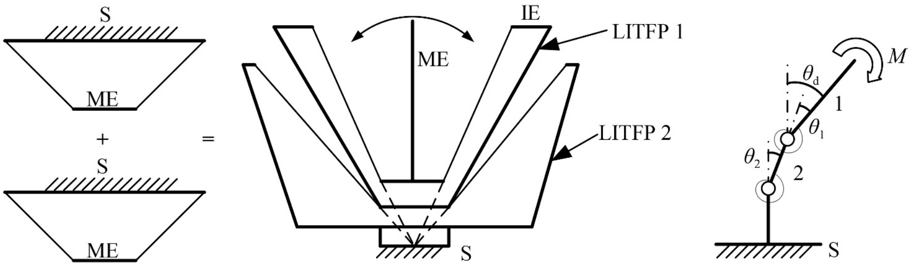

(a) (b)

Fig. 3 Pseudo-rigid body model of the double leaf-type isosceles-trapezoidal flexural pivot (D-LITFP): (a) structure design of the D-LITFP and (b) equivalent pseudo-rigid body model of the D-LITFP.

where K_1 and K_2 are the bending stiffness of LITFPs 1 and 2, respectively.

From Eq. (18), we have

$$\frac{\theta_1}{\theta_2} = \frac{K_2}{K_1}. \tag{19}$$

According to Eq. (12), the stiffness of LITFPs 1 and 2 can be obtained:

$$K_1 = \frac{8EI_1(H_1^2 + H_1h_{f1} + h_{f1}^2)\cos\varphi_1}{(H_1 - h_{f_1})^3}, \tag{20}$$

$$K_2 = \frac{8EI_2(H_2^2 + H_2h_{f2} + h_{f2}^2)\cos\varphi_2}{(H_2 - h_{f2})^3}, \tag{21}$$

where I_i, H_i (i = 1,2), and other parameters are configuration parameters of LITFPs 1 and 2, respectively, with the same meaning as above.

By combining Eqs. (17)–(19), we have

$$\theta_d = \left(1 + \frac{K_1}{K_2}\right)\theta_1 = \frac{K_1 + K_2}{K_1K_2}M. \tag{22}$$

Then, the stiffness K_d of the D-LITFP is

$$K_d = \frac{K_1K_2}{K_1 + K_2}. \tag{23}$$

Thus, the stiffness K_V of the VCM mechanism is

$$K_V = 2K_d = \frac{2K_1K_2}{K_1 + K_2}. \tag{24}$$

For the maximum stress $\sigma_{d\max}$ of the D-LITFP, the larger value of the maximum stress of the two LITFPs should be taken, that is,

$$\sigma_{d\max} = \max\{\sigma_{1\max}, \sigma_{2\max}\}, \tag{25}$$

where $\sigma_{1\max}$ and $\sigma_{2\max}$ are the maximum stress values corresponding to rotation angles of LITFPs 1 and 2, which can be obtained by Eq. (15), respectively.

Similarly, the maximum rotation angles $\theta_{1\max}$ and $\theta_{2\max}$ of LITFPs 1 and 2 can be obtained by Eq. (16), if

$$\theta_{1\max} > \frac{K_2}{K_1}\theta_{2\max}. \tag{26}$$

The maximum stress of LITFP 2 is the first to reach yield strength (S_y). In this case, the maximum bending angle $\theta_{d\max}$ is

$$\theta_{d\max} = \frac{K_1 + K_2}{K_1}\theta_{2\max} = \frac{K_1 + K_2}{K_1}\frac{H_2}{Et_2n_2(3n_2 - 1)\cos\varphi_2}S_y. \tag{27}$$

Otherwise,

$$\theta_{d\max} = \frac{K_1 + K_2}{K_2}\theta_{1\max} = \frac{K_1 + K_2}{K_2}\frac{H_1}{Et_1n_1(3n_1 - 1)\cos\varphi_1}S_y. \tag{28}$$

That is,

$$\theta_{d\max} = \min\left\{\frac{K_1 + K_2}{K_1}\theta_{2\max}, \frac{K_1 + K_2}{K_2}\theta_{1\max}\right\}, \tag{29}$$

where t_i and n_i (i = 1, 2) are the same as those of t and n above.

When the two LITFP components of D-LITFP reach the maximum rotation angle, the following equation needs to be satisfied:

$$\theta_{1\max} = \frac{K_2}{K_1}\theta_{2\max}. \tag{30}$$

That is,

$$\frac{K_1H_1}{t_1n_1(3n_1 - 1)\cos\varphi_1} = \frac{K_2H_2}{t_2n_2(3n_2 - 1)\cos\varphi_2}. \tag{31}$$

2.4 Parameter determination

The stiffness and rotation angle of the VCM mechanism can be changed by optimizing its structural parameters. The influence of each parameter change on the overall structural performance needs to be verified to obtain a reasonable rotational stiffness and maximum rotation angle. For LITFP 1, its structural parameters are preliminarily set as H_1 = 55 mm, h_{f1} = 17 mm, φ_1 = 10°, b = 10 mm, and t = 1.0 mm. Figure 4 shows the change in stiffness K with the structural parameters (width b, thickness t, height H, h_f, and included angle φ of the leaf). The results show that, when other parameters remain

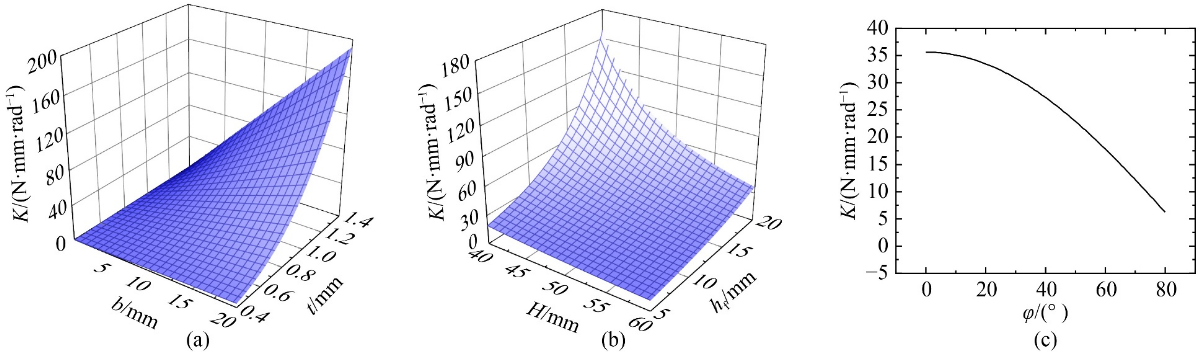

(a) (b) (c)

Fig. 4 Influence of each parameter change on the stiffness: (a) change in stiffness K with the width b and thickness t, (b) change in stiffness K with height H and h_f, and (c) change in stiffness K with the included angle φ of the leaf.

unchanged: (i) The stiffness K is proportional to b, t, and h_f and inversely proportional to H and φ; among them, the influence of φ and b on stiffness K is slight; (ii) the stiffness K is inversely proportional to H/h_f. Therefore, a certain performance index ($\theta_{\max} \approx 15°$) is used as the guide for the structure design, and the thickness t and H/h_f are mainly considered, while the parameters φ and width b are supplemented by the trial-and-error method for parameter selection. Among them, the parameter φ can be used to ensure that the bending angle of the VCM mechanism is not limited by the opening angle of its V-shape structures. Therefore, the structural parameters of the two LITFPs can be determined as shown in Table 1. The stiffness values of the two LITFPs are $K_1 = 6.97$ N·m/rad and $K_2 = 6.88$ N·m/rad, and the maximum strokes are $\theta_{1\max} = 7.11°$ and $\theta_{2\max} = 7.13°$. Furthermore, the composite stiffness and the maximum stroke of the designed VCM mechanism are $K_V = 6.92$ N·m/rad and $\theta_{d\max} = 14.2°$, respectively, as shown in Table 2.

3 Kinematic analysis

In this chapter, a complete kinematic model is established, including the relationships between the difference in driving cables length and the bending configuration of the proposed VCM mechanism (we call the VCM mechanism a half joint, which can be simplified as a single-axis rotating pivot), single-joint, and single-segment, as well as the relationship between the bending configuration of each segment and the end pose of the whole continuum robot. The process is shown in Fig. 5. In each section, the basic symbols $\Delta l(i)$, θ, and η are used to represent the cable length difference, bending angle, and bending direction, respectively, to make the formula more concise. The specific symbols are shown in Table 3.

Table 1 Characteristic parameters of the two LITFPs

Type	t/mm	b/mm	H/mm	h_f/mm	φ/(°)	K/(N·m·rad^{-1})	$\theta_{\max}$/(°)
LITFP 1	0.6	9	55	17	12	6.97	7.11
LITFP 2	0.6	9	46	14	34	6.88	7.13

Table 2 Characteristic parameters of the VCM mechanism

Type	Length	Diameter	K_V	$\theta_{d\max}$
VCM mechanism	66 mm	115 mm	6.92 N·m/rad	14.2°

3.1 Kinematic analysis of single joint

For the designed continuum robot, each joint requires 2 degrees of freedom. Considering that the half joint only has 1 degree of freedom, every two half joints can form an independent functional joint. The combination mode is shown in Fig. 6(a). The rotation axes of the two half joints are on the same plane and perpendicular to each other. This arrangement means that the phase difference of the rotation axis is 90°, which forms a joint similar to the Hooke hinge in function. Moreover, the rotation angles of the two half joints are set as φ_1 and φ_2, respectively (Fig. 6(b)).

Through the Denavit–Hartenberg parameter method, the pose transformation matrix can be obtained from Fig. 6(b).

$$ {}^{2}_{0}\boldsymbol{T} = {}^{1}_{0}\boldsymbol{T}\,{}^{2}_{1}\boldsymbol{T} = \begin{bmatrix} \cos\varphi_2\cos\varphi_1 & \sin\varphi_2\cos\varphi_1 & -\sin\varphi_1 & 0 \\ \cos\varphi_2\sin\varphi_1 & \sin\varphi_2\sin\varphi_1 & \cos\varphi_1 & 0 \\ \sin\varphi_2 & -\cos\varphi_2 & 0 & 0 \\ 0 & 0 & 0 & 1 \end{bmatrix}, \qquad (32)$$

where ${}^{i}_{j}\boldsymbol{T}$ represents the coordinate transformation of coordinate system $\{O_i\}$ with respect to coordinate system $\{O_j\}$.

As shown in Fig. 6(b), the relationship between rotation angles (φ_1 and φ_2) of two half joints and joint configurations (θ_{joint} and η_{joint}) is

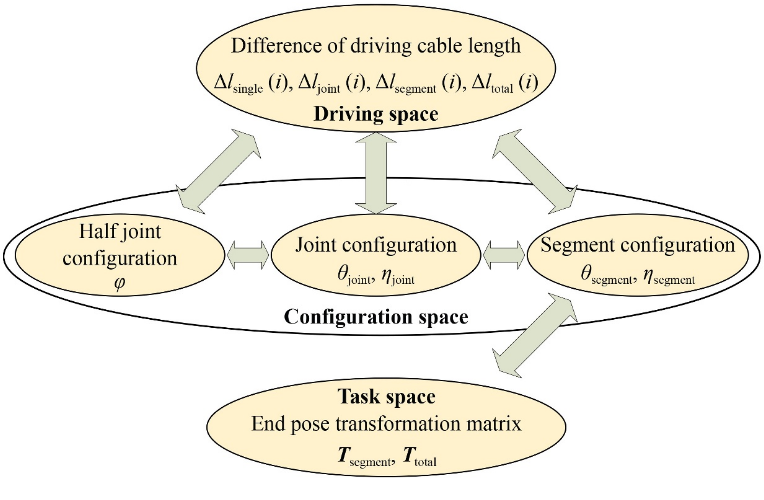

Fig. 5 Mappings among driving space, configuration space, and task space.

Table 3 Symbol description table

Symbol	Description
$l_{\text{single}}(i)$	Driving cable length in half joint
$\Delta l_{\text{single}}(i)$	Difference in driving cable length in half joint
$l_{\text{joint}}(i)$	Driving cable length in single joint
$\Delta l_{\text{joint}}(i)$	Difference in driving cable length in single joint
$l_{\text{segment}}(i)$	Driving cable length in a single segment
$\Delta l_{\text{segment}}(i)$	Difference in driving cable length in a single segment
$l_{\text{total}}(i)$	Driving cable length of the whole continuum robot
$\Delta l_{\text{total}}(i)$	Difference in driving cable length of the whole continuum robot
φ	Bending angle of the half joint
$\theta_{\text{joint}}, \eta_{\text{joint}}$	Bending angle and bending direction of the single joint
$\theta_{\text{segment}}, \eta_{\text{segment}}$	Bending angle and bending direction of the single segment
$\boldsymbol{T}_{\text{segment}}$	Pose transformation matrix of the single segment
$\boldsymbol{T}_{\text{total}}$	End pose transformation matrix of the whole continuum robot

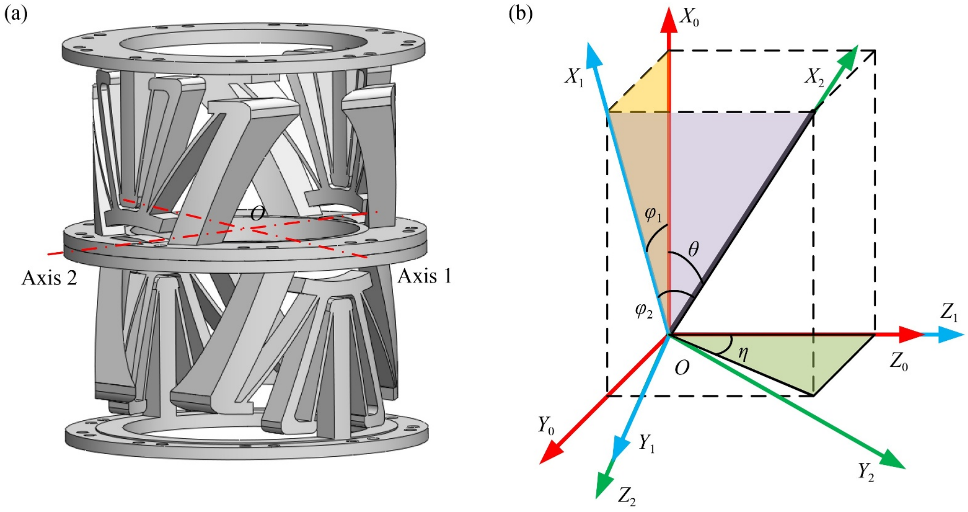

Fig. 6 Design of the flexural joint: (a) combination mode of half joint and (b) coordinate transformation of half joint.

$$\begin{cases}\sin\varphi_2 = \sin\theta_{\text{joint}}\cos\eta_{\text{joint}},\\ \sin\theta_{\text{joint}}\sin\eta_{\text{joint}} = \sin\varphi_1\cos\varphi_2,\\ \cos\theta_{\text{joint}} = \cos\varphi_1\cos\varphi_2.\end{cases} \tag{33}$$

According to Eq. (33), the mapping relationship is

$$\begin{aligned}&\varphi_1 = \arctan(\tan\theta_{\text{joint}}\sin\eta_{\text{joint}}),\\ &\varphi_2 = \arcsin(\sin\theta_{\text{joint}}\cos\eta_{\text{joint}}),\\ &(\varphi_1, \varphi_2 \in [-14°,\ 14°]),\end{aligned} \tag{34}$$

$$\begin{aligned}&\theta_{\text{joint}} = \arccos(\cos\varphi_1\cos\varphi_2),\\ &\eta_{\text{joint}} = \arctan\frac{\sin\varphi_1}{\tan\varphi_2},\\ &(\theta_{\text{joint}} \in [-14°,\ 14°],\ \eta_{\text{joint}} \in [0°,\ 360°]).\end{aligned} \tag{35}$$

Figure 7(a) shows the relationship between cable length difference and rotation angle φ of half joint. Point P_{i0} is defined as the position of the cable in the lower plate, P_i is the position of the corresponding cable in the upper plate, and P_i' is the position of the cable in the upper plate after bending. The cable length $l_{\text{single}}(i) = |P_{i0}P_i'|$. The assumption is that each driving cable is parallel, that is, the bending angle of each driving cable is φ. The rotation angle φ can be expressed as

$$\varphi = \arcsin\frac{\Delta l_{\text{single}}(i)}{r\sin\dfrac{2\pi(i-1)}{9}}, \tag{36}$$

where i indicates the number of cables, and r is the radius of the circle where the driving cable is located. Figure 7(b) shows the distribution location and number of driving cables. The driving cable that passes through the

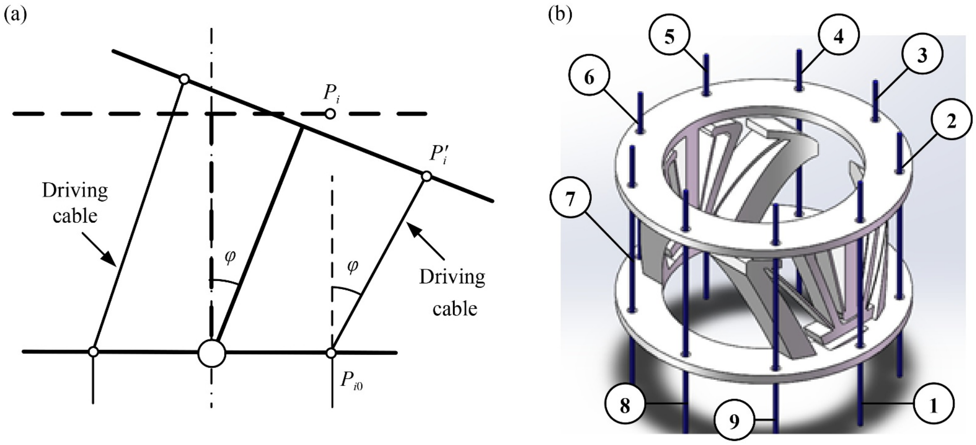

Fig. 7 Half joint: (a) analytical model of cable length difference for half joint and (b) distribution, and a serial number of driving cables (uniform distribution). Each segment is driven by three evenly distributed driving cables, of which Nos. 1, 4, and 7 driving cables are the first group, Nos. 2, 5, and 8 driving cables are the second group, and Nos. 3, 6, and 9 driving cables are the third group.

half joint rotating shaft is set as No. 1, and then, it is numbered counterclockwise.

When θ_{joint} and η_{joint} are known (inverse solution), the length of the driving cable can be obtained indirectly from the bending angles of the two half joints. However, the bending angles of the two half joints cannot be obtained directly from the difference in the cable length in the joint given that the distribution of the driving cable length in the two half joints of a single joint cannot be controlled. Therefore, the relationship between the difference in the cable length $\Delta l_{\text{joint}}(i)$ and the bending angles (φ_1, φ_2) needs to be resolved.

When the driving cable of group i is driven, the following equations can be listed.

$$\begin{cases} r\sin\dfrac{2(i-1)\pi}{9}\sin\varphi_1 \\ \quad +r\sin\left(\dfrac{2(i-1)\pi}{9}-\dfrac{\pi}{2}\right)\sin\varphi_2=\Delta l_{\text{joint}}(i), \\ r\sin\dfrac{2(i+2)\pi}{9}\sin\varphi_1 \\ \quad +r\sin\left(\dfrac{2(i+2)\pi}{9}-\dfrac{\pi}{2}\right)\sin\varphi_2=\Delta l_{\text{joint}}(i+3), \\ r\sin\dfrac{2(i+5)\pi}{9}\sin\varphi_1 \\ \quad +r\sin\left(\dfrac{2(i+5)\pi}{9}-\dfrac{\pi}{2}\right)\sin\varphi_2=\Delta l_{\text{joint}}(i+6). \end{cases} \tag{37}$$

Any two of these equations are solved.

$$\sin\varphi_1=\frac{\sin\left(\dfrac{2(i-1)\pi}{9}-\dfrac{\pi}{2}\right)\Delta l_{\text{joint}}(i+3)-\sin\left(\dfrac{2(i+2)\pi}{9}-\dfrac{\pi}{2}\right)\Delta l_{\text{joint}}(i)}{r\sin\dfrac{2(i+2)\pi}{9}\sin\left(\dfrac{2(i-1)\pi}{9}-\dfrac{\pi}{2}\right)-r\sin\dfrac{2(i-1)\pi}{9}\sin\left(\dfrac{2(i+2)\pi}{9}-\dfrac{\pi}{2}\right)}, \tag{38}$$

$$\sin\varphi_2=\frac{\sin\dfrac{2(i+2)\pi}{9}\Delta l_{\text{joint}}(i)-\sin\dfrac{2(i-1)\pi}{9}\Delta l_{\text{joint}}(i+3)}{r\sin\dfrac{2(i+2)\pi}{9}\sin\left(\dfrac{2(i-1)\pi}{9}-\dfrac{\pi}{2}\right)-r\sin\dfrac{2(i-1)\pi}{9}\sin\left(\dfrac{2(i+2)\pi}{9}-\dfrac{\pi}{2}\right)}. \tag{39}$$

The bending angle and bending direction of the joint can be deduced by Eq. (35).

3.2 Kinematic analysis of continuum robot

For the kinematic relationship of the single-segment robot, the single-segment continuum robot is assumed to bend uniformly based on piecewise constant curvature theory. Thus, the single-segment continuum robot can be simplified into the model shown in Fig. 8. According to the bending properties of a single segment, the center of the lower and upper surface of each joint is on the same arc, and the center of the arc falls on the bending plane and the lower surface of the first joint, with a radius of $R_{\text{bend}}=l_{\text{single}}\Big/\tan\dfrac{\theta_{\text{joint}}}{2}$ (Fig. 8(a)). O and A have 2 degrees of freedom.

First, each rotation axis is determined. Then, it is defined as the Z-axis. Finally, the X-axis is determined according to the vertical relationship. According to the

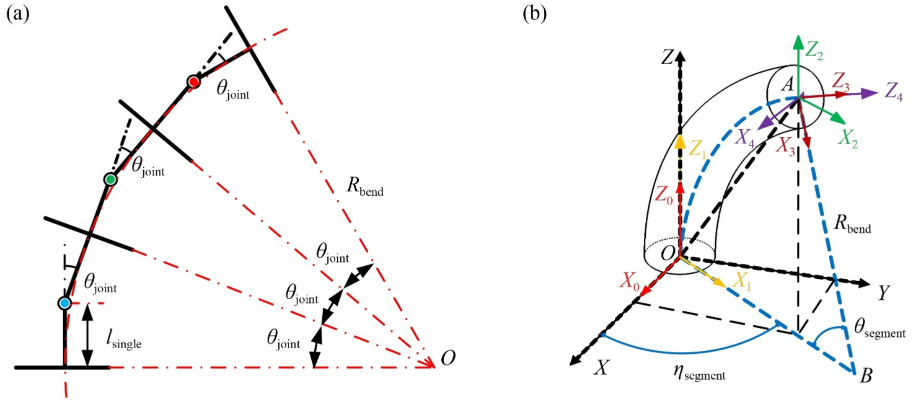

Fig. 8 Schematic of single-segment bending: (a) bending plane and (b) coordinate transformation.

geometric relationship and the properties of the continuum robot, the coordinate transformation (point A relative to point O) of the end poses in the coordinate system $\{XYZ\}$ can be calculated. The pose matrix of each segment also needs to be adjusted by rotating $-\eta$ around axis Z_3, as shown in Fig. 8(b).

$$\boldsymbol{T}_{\text{segment}} = \begin{bmatrix} {}^4_0\boldsymbol{R} & {}^4_0\boldsymbol{P} \\ \boldsymbol{0}_{1\times3} & 1 \end{bmatrix}$$

$$= \begin{bmatrix} \boldsymbol{R}_Z(\eta) & 0 \\ \boldsymbol{0}_{1\times3} & 1 \end{bmatrix} \begin{bmatrix} \boldsymbol{R}_Y(\theta) & \begin{matrix} R(1-\cos\theta) \\ 0 \\ R\sin\theta \end{matrix} \\ \boldsymbol{0}_{1\times3} & 1 \end{bmatrix} \begin{bmatrix} \boldsymbol{R}_Z(-\eta) & 0 \\ \boldsymbol{0}_{1\times3} & 1 \end{bmatrix}, \tag{40}$$

where R is the bending radius $\boldsymbol{R}_{\text{bend}}$, θ is the bending angle θ_{segment}, and η is the bending direction angle η_{segment} of the segment. ${}^4_0\boldsymbol{R}$ and ${}^4_0\boldsymbol{P}$ are the rotation matrix and displacement vector from $\{O_4\}$ to $\{O_0\}$, respectively. $\boldsymbol{R}_Y(\theta)$ represents the rotation matrix which rotated at a certain angle θ around the Y-axis. $\boldsymbol{R}_Z(\eta)$ means the same thing.

Then, the pose matrix $\boldsymbol{T}_{\text{total}}$ of the whole continuum robot is

$$\boldsymbol{T}_{\text{total}} = \prod_i^n \boldsymbol{T}^i_{\text{segment}}. \tag{41}$$

4 Performance validation

To validate the validity and accuracy of the PRB model, finite element analysis (FEA) and experiments, including the validation of the compressive strength, the stiffness, and the stroke of the VCM mechanism, are conducted. Furthermore, the motion performance of the continuum robot is tested.

4.1 Finite element analysis

The cables can only provide tension in practical applications. Thus, the joints of the continuum robot are in a state of compression, which places great demands on their strength and stability. The axial compressive strength of the VCM mechanism, which is determined by its yield strength, can be verified by FEA, as shown in Fig. 9. Its structural parameters are consistent with those shown in Table 1. In the simulation, the lower surface of the VCM mechanism is fixed, and a uniform force of 1800 N perpendicular to the upper surface is applied. The maximum stress received by the leaf is 450.58 MPa, which is approximately equal to the yield strength of the leaf material: aluminum alloy (Al alloy, yield strength: 455 MPa), as shown in Fig. 9(a). The maximum stress of the VCM mechanism also occurs in the excessive position between the leaf and the stand, which belongs to the phenomenon of stress concentration and conforms to the general law. Therefore, the overall axial compressive capacity of the VCM mechanism is approximately 1800 N. The deformation in Fig. 9(b), which is symmetrically distributed on both sides of the rotation axis of the VCM mechanism, is mainly reflected on the upper surface and the tensioned leaves. The maximum axial deformation is 0.94 mm, which appears on the upper surface farthest from the rotating axis. Thus, the axial stiffness is approximately 1915 N/mm, and the deformation ratio is approximately 1.42% (the length $l_{\text{single}} = 66$ mm).

On this basis, the stiffness K and stroke θ of the VCM mechanism are verified by FEA. As shown in Figs. 10(a) and 10(b), the stiffness calculation and simulation results of LITFPs 1 and 2 exhibit great consistency, especially LITFP 2, which is related to the included angle φ_2 of the leaf to a certain extent. Figure 10(c) shows the relative error of stiffness for LITFPs 1 and 2. First, the simulation result is assumed to be closer to the real value. The relative error ε of PRB model with respect to FEA is defined as

$$\varepsilon = \frac{|r_{\text{f}} - r_{\text{p}}|}{r_{\text{f}}}, \tag{42}$$

where r_{f} is the result of FEA, and r_{p} is the calculation result of the PRB model. The accuracy of the calculation

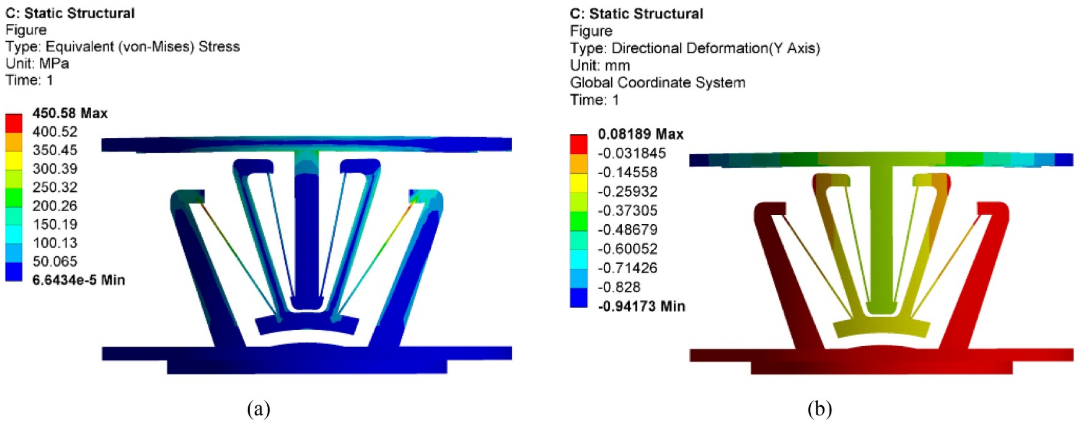

Fig. 9 Axial stiffness simulation of virtual-center of motion mechanism: (a) equivalent stress and (b) axial deformation.

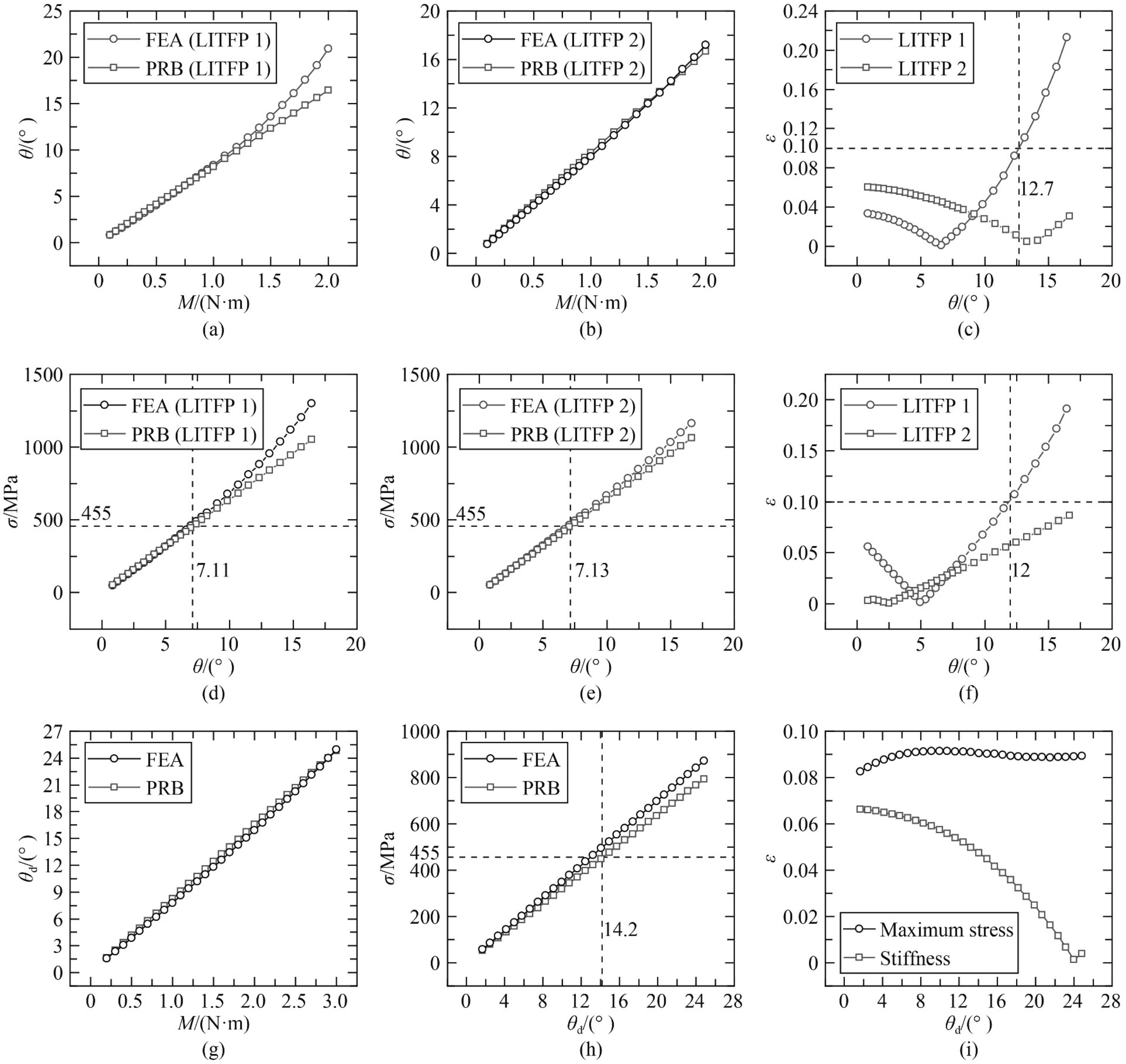

Fig. 10 Finite element analysis (FEA): (a) FEA and pseudo-rigid body (PRB) values of stiffness for LITFP 1, (b) FEA and PRB values of stiffness for LITFP 2, (c) relative errors of stiffness for LITFPs 1 and 2, (d) FEA and PRB values of maximum stress for LITFP 1, (e) FEA and PRB values of maximum stress for LITFP 2, (f) relative errors of maximum stress for LITFPs 1 and 2, (g) FEA and PRB values of stiffness for virtual-center of motion (VCM) mechanism, (h) FEA and PRB values of maximum stress for VCM mechanism, and (i) relative errors of stiffness and maximum stress for VCM mechanism. LITFP: leaf-type isosceles-trapezoidal flexural pivot.

result is acceptable when the relative error is less than 10%.

Figure 10(c) shows that, when the rotation angles of LITFPs 1 and 2 are within 12.7°, the relative errors of stiffness for the two LITFPs are less than 10%. Thus, the calculated values of stiffness for the PRB model are available. Then, the maximum stress values of LITFPs 1 and 2 at corresponding rotation angles are compared, as shown in Figs. 10(d)–10(f). The results show that the relative errors of maximum stress for the two LITFPs are also less than 10% when the rotation angles of LITFPs 1 and 2 are within 12°. Similarly, the stiffness and maximum stress of the VCM mechanism are verified, as shown in Figs. 10(g)–10(i). The relative errors of stiffness and the maximum stress are within 10%. Thus, the maximum stroke θ_{dmax} = 14.2° of the VCM mechanism can be reached. It demonstrates the accuracy and validity of the PRB model of LITFP.

4.2 Experimental validation

As shown in Fig. 11(a), the stiffness experimental device of the VCM mechanism is installed on the vibration isolation platform. The device is mainly composed of a lead screw slide, force sensor (YISIDA: DS2-100N; Accuracy: ±0.2% Full Scale), displacement sensor (Keyence: LK-H050; Accuracy: ±0.02% Full Scale), and voltage stabilized power supply. Among them, the lead screw slide is fixed on the vibration isolation platform and the hand wheel is installed above the slide. The force sensor is fixed on the lead screw slide and its displacement can be applied by rotating the hand wheel. The laser displacement sensor is used to monitor the moving distance for measuring the displacement of the lead screw slide more accurately.

The experimental object is the VCM mechanism processed by 3D printing (material: polylactic acid (PLA)), as shown in Fig. 11(b). To demonstrate that the 3D printed sample can be used for experimental validation instead of the designed VCM mechanism (material: Al alloy), two conditions need to be satisfied: (i) The range of motion (maximum bending angle) of the 3D printed sample is not smaller than that of the Al alloy sample; (ii) the PRB model is also applicable to the stiffness modeling analysis of the 3D printed sample. In the abovementioned conditions, condition (i) is used to verify that the configuration can reach the designed maximum bending angle without the leaves being pulled off. Without considering the limitation of V-shape structures, the data in Table 4 show that the VCM mechanism made of PLA can reach a maximum bending angle of 29.6°. Furthermore, the maximum bending angles of the two LITFPs are 14.79° and 14.83°, respectively. These angles are larger than those of the VCM mechanism made of Al alloy. Condition (ii) and the VCM mechanism's configuration together ensure the accuracy of the motion of the mechanism.

The thickness of the printed leaf is selected as t = 1.0, 1.2, and 1.4 mm due to the limitation of processing technology. The stiffness of the experimental samples can be calculated as

$$K = \frac{Fr}{\arctan\dfrac{\Delta l}{r}}, \tag{43}$$

where r is the vertical distance between the force F and the rotating axis, and Δl is the displacement of the force sensor.

At least five sets of F values and Δl values are taken for each experiment, and the average value of the experiments is taken as the measured stiffness of the VCM mechanism, as shown in Fig. 12. The trend of the experimental stiffness of the samples is consistent with that of the calculated stiffness of the PRB model, and the difference is stable within a certain range. The reason is that a certain difference exists between the elastic modulus of different types of PLA materials and the standard value. It also shows that the stiffness of the 3D printed sample can also be analyzed by the PRB model. Therefore, the 3D printed sample can be used as a substitute for the experimental validation from the results in Table 4 and Fig. 12.

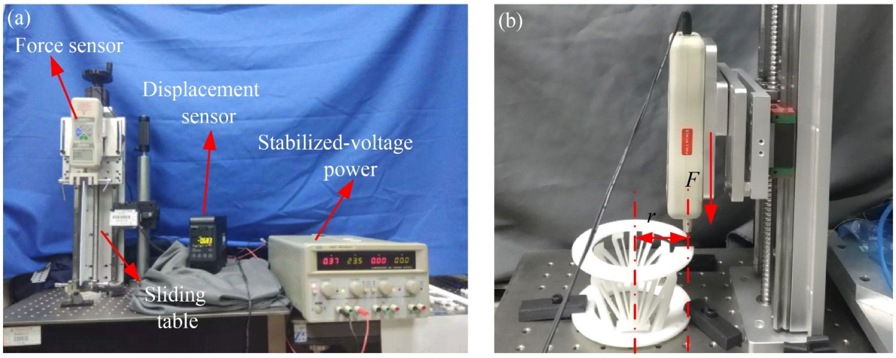

Fig. 11 Stiffness experiment of virtual-center of motion mechanism: (a) experimental device and (b) experimental scene.

Table 4 Comparison of the performance of the VCM mechanism for two different materials.

Type	Material	E/GPa	S_y/MPa	K/(N·m·rad^{-1})	$\theta_{\max}$/(°)
LITFP 1	Al alloy	71	455	6.97	7.11
	PLA	3	40	0.29	14.79
LITFP 2	Al alloy	71	455	6.88	7.13
	PLA	3	40	0.29	14.83
VCM	Al alloy	71	455	6.92	14.20
	PLA	3	40	0.29	29.60

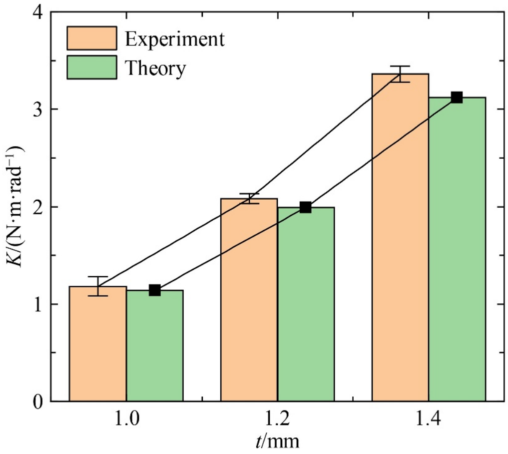

Fig. 12 Trend of experimental stiffness and theoretical calculation stiffness of samples (t = 1.0, 1.2, and 1.4 mm).

4.3 Kinematic performance

The workspace of the continuum robot is a vital criterion for evaluating its property. The previous section indicates that the bending range of each VCM mechanism is ±14.2°. The assumption is that the continuum robot has three segments, each consisting of three flexible joints (six VCM mechanisms). Therefore, the range of bending angle of the single segment can be set to ±42°, and the range of the bending direction of the single segment is [0, 2π]. Figure 13 shows the several different workspaces of the continuum robot (single-segment, two-segment, and three-segment) according to Eq. (41).

The instrument (DXL digital angle ruler) is used to measure the pose (θ and η) during motion for further evaluating the motion performance of the continuum robot. First, the DXL digital angle ruler is fixed on the end plane of the continuum robot. In the initial state ($\theta = 0$, $\eta = 0$, Fig. 14(a)), the horizontal installation direction of the DXL digital angle ruler is set to the X-axis and the axis direction of the continuum robot is set to the Y-axis. Then, the motion pose of the continuum robot can be calculated by measuring the dual-axis tilt angle (φ_X and φ_Y) at each position.

$$\begin{cases} \theta = \arcsin \sqrt{\sin^2\varphi_X + \sin^2\varphi_Y}, \\ \eta = \arctan \dfrac{\sin\varphi_X}{\sin\varphi_Y}. \end{cases} \tag{44}$$

The prototype of the continuum robot is shown in Fig. 14(a). It has three segments, and each segment is composed of two flexural joints, that is, four VCM mechanisms. Therefore, the maximum bending angle of the whole continuum robot is approximately 84°, as shown in Fig. 14(b). The continuous robot can also perform S-shape bending (Fig. 14(c)). The continuum robot is controlled to complete a uniform circular motion shown in Fig. 14(d). In this process, the preset bending direction and bending angle can be used as the input values by the control system, and several positions are selected to compare the input values with the actual values (measured values). The selected positions are shown in Table 5.

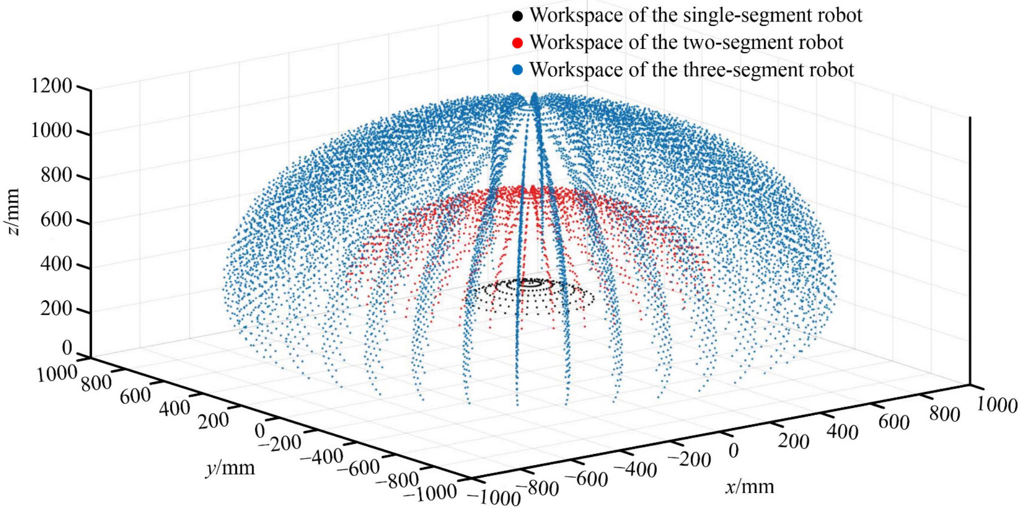

Fig. 13 Workspaces of the continuum robot.

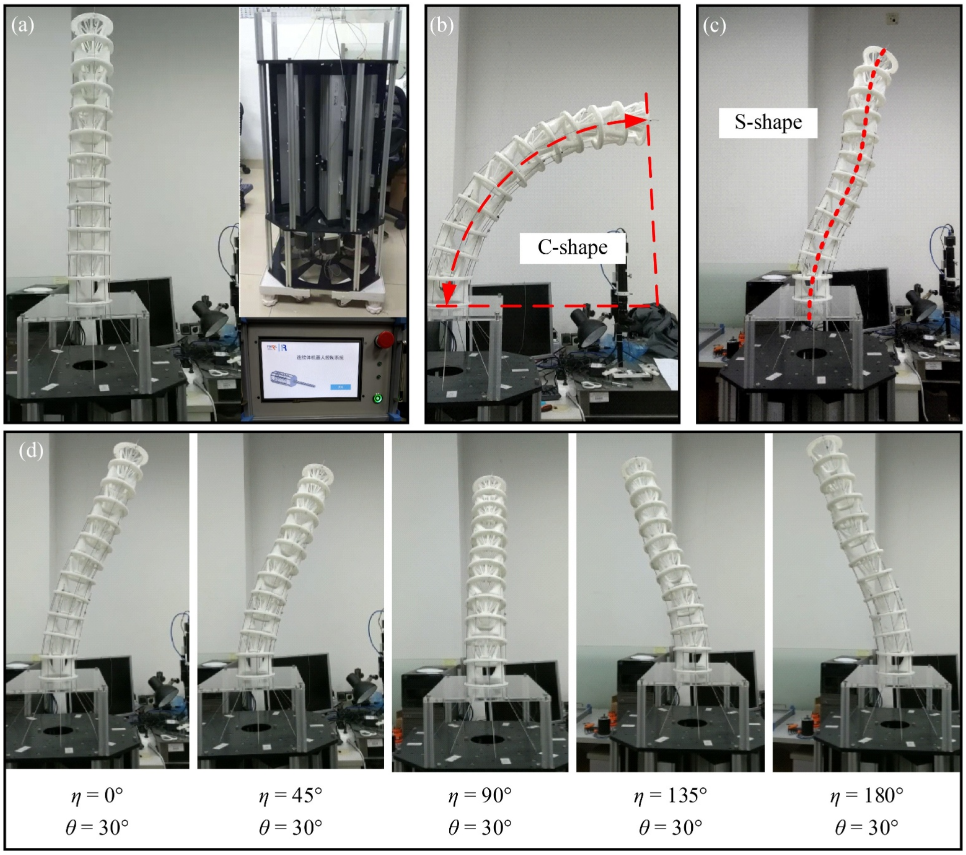

η = 0° θ = 30°
η = 45° θ = 30°
η = 90° θ = 30°
η = 135° θ = 30°
η = 180° θ = 30°

Fig. 14 Motion performance of the continuum robot: (a) prototype and control system of continuum robot, (b) C-shape, (c) S-shape, and (d) uniform circular motion (0° – 180°).

Table 5 Repeatable positioning accuracy experiment arrangement

Number	Bending angle, θ/(°)	Bending direction, η/(°)
0	30	0
1	30	30
2	30	60
3	30	90
4	30	120
5	30	150
6	30	180

The results in Fig. 15 show that the repeatable positioning accuracies of the bending angle of the continuum robot are approximately ±0.11° (η = 0°), ±0.53° (η = 30°), ±0.36° (η = 60°), ±0.67° (η = 90°), ±0.73° (η = 120°), ±0.43° (η = 150°), and ±0.05° (η = 180°) for the respective bending direction angles (Fig. 15(a)). The maximum repeatable positioning accuracy of the continuum robot is ±0.73° for the same bending direction angle. However, for the whole bending direction angle (θ = 0°−180°), the maximum repeatable positioning accuracy of the continuum robot can still reach ±1.47° at the bending angle, and the maximum deviation of the bending angle is approximately 1.5° (Fig. 15(c)). The repeatable positioning accuracies of the continuum robot at the bending direction angle are approximately ±2.12° (η = 0°), ±0.70° (η = 30°), ±0.50° (η = 60°), ±1.82° (η = 90°), ±2.46° (η = 120°), ±0.71° (η = 150°), and ±1.74° (η = 180°) at a bending angle of 30° (Fig. 15(b)). Therefore, the maximum repeatable positioning accuracy of the bending direction is ±2.46°, and the maximum deviation is approximately 3.81° (Fig. 15(d)). The results show that the repeatable positioning accuracy of the continuum robot is acceptable. The experimental error mainly comes from the assumption in Section 3.2: The single-segment continuum robot bends uniformly which ignores the self-weight and payload of the continuum robot. When the load is ignored, the bending stiffness of the joint needs to offset the influence of the bending moment caused by its weight to achieve the uniform bending of the continuum robot. Therefore, the stiffness of each VCM mechanism constituting the continuum robot can be considered to increase sequentially, rather than equally, to offset the effect of self-weight in subsequent studies.

5 Discussion

The V-shape structures are unavoidable for the VCM mechanism, but they do not limit the bending angle of the

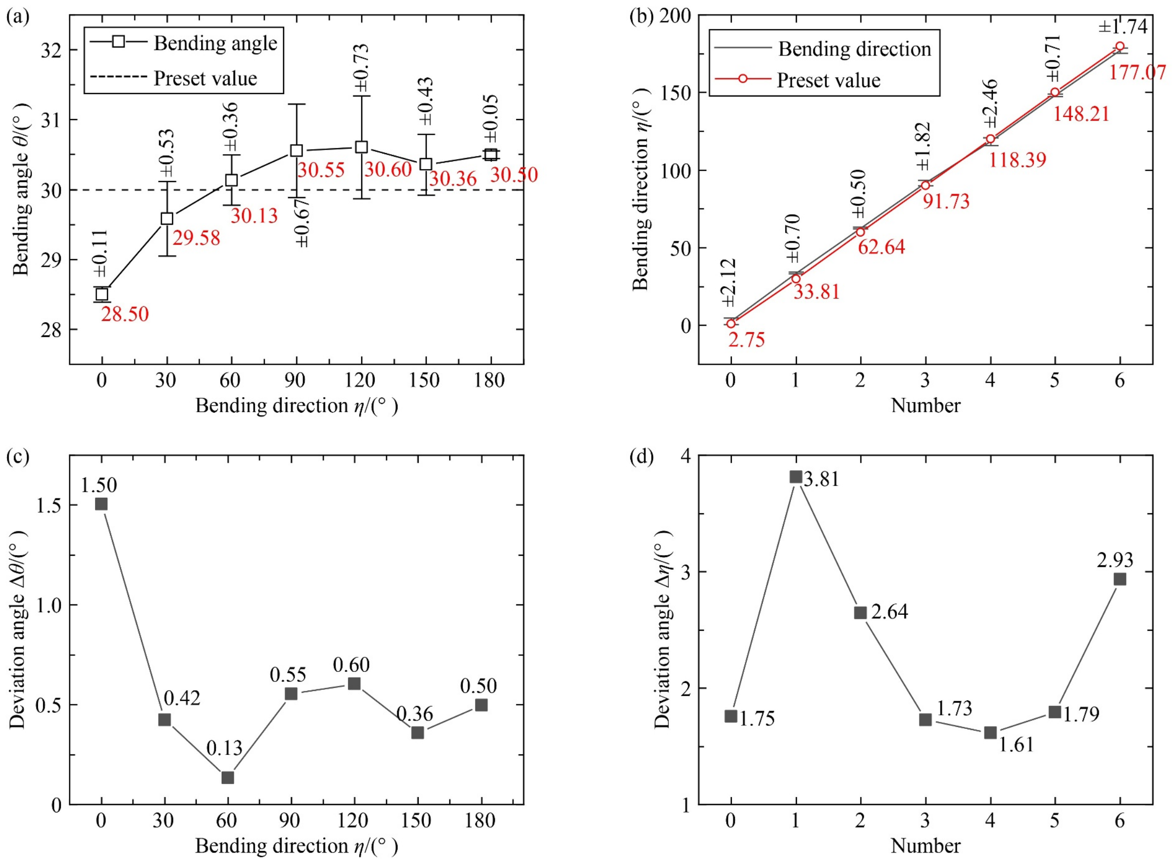

Fig. 15 Repeatable positioning accuracy experiment: repeatable positioning accuracy of (a) bending angle and (b) bending direction; deviation angle of (c) bending angle and (d) bending direction.

mechanism. First, when LITFPs receive pressure, they can be divided into two types depending on the state of the leaf: compressed leaf-type isosceles-trapezoidal flexural pivots (CLITFPs) and tensioned leaf-type isosceles-trapezoidal flexural pivots (TLITFPs). The CLITFP is easily destabilized when under pressure and cannot withstand large axial pressure due to the structural characteristics of the leaf itself. By comparison, the axial pressure resistance of the TLITFP has a greater advantage, but it also determines its structural characteristics (V-shape structure): Its bending angle will be limited to a certain extent by its structure. However, according to the conclusions mentioned in Section 2.4, the parameter φ, which has a small effect on the stiffness of the VCM mechanism, can be used to ensure that the bending angle of the VCM mechanism is not limited by the opening angle of its V-shape structures as much as possible. Second, the V-shape structure is composed of two parts: the ME and IE. The IE (with minimal deformation) can be considered a rigid element. These rigid elements can also provide a limiting and protective effect when the VCM mechanism is bent to its maximum bending angle. This condition prevents the VCM mechanism from continuing to bend to the point where the leaves are pulled off. Overall, the advantages of the V-shape construction outweigh the disadvantages when the extreme bending angle of the structure is not required.

Meanwhile, the complexity of the structure and its miniaturization is a major conflict in structural design. The VCM mechanism designed is formed using D-LITFPs, which limit its miniaturization to some extent. In subsequent studies, the miniaturized design of the VCM mechanism will be the focus of our research, and a miniaturized VCM mechanism with a diameter of 40 mm will be proven feasible. A continuum robot of this size should be adequate for applications in the most complex, constrained scenarios (other than minimally invasive surgery), such as the maintenance of aerospace, space, and nuclear power plants.

6 Conclusions

A continuum robot based on the VCM mechanism is designed in this study. The robot takes the VCM mechanism as the flexural joint and integrates the advantages of the VCM mechanism into the joint design. In this way, the flexural joint can be processed integrally to be free from assembly and has a fixed axis of rotation. This design simplifies the kinematics modeling of the continuum robot. It also has a considerable stiffness to ensure the uniformity of bending deformation. The D-LITFP which can rotate at a larger stroke is adopted as the main configuration of the VCM mechanism, and its main principle is to connect LITFPs in series in the same direction to increase its rotation angle and then in parallel to increase its stiffness.

In the whole continuum robot, every two VCM mechanisms (diameter: 115 mm, length: 66 mm) can form a flexural joint with 2 degrees of freedom and one fixed rotation axis. The length of the whole robot is 792 mm, which is composed of 3 segments and 12 VCM mechanisms in series (each segment has 2 flexural joints), and its length–diameter ratio is approximately 7. Moreover, the length–diameter ratio can be changed by the number of VCM mechanisms in series. In the performance analysis of the VCM mechanism and continuum robot, the axial compressive stiffness of the VCM mechanism is approximately 1915 N/mm, which can bear the pressure of at least 1800 N. The maximum stroke (bending angle) of the flexural joint can reach 14.2°, and the composite stiffness is approximately 6.92 N·m/rad. The repeatable positioning accuracies of the continuum robot are approximately ±1.47° (bending angle) and ±2.46° (bending direction). In the later stage, the stiffness of each joint within the segment should be different to balance the influence of weight and load on the whole stiffness for realizing the uniform bending of the continuum robot.

Nomenclature

Abbreviations

Al alloy	Aluminum alloy
CLITFP	Compressed leaf-type isosceles-trapezoidal flexural pivot
D-LITFP	Double leaf-type isosceles-trapezoidal flexural pivot
FEA	Finite element analysis
ICR	Instantaneous center of rotation
IE	Intermediate element
LITFP	Leaf-type isosceles-trapezoidal flexural pivot
ME	Movement element
PLA	Polylactic acid
PRB	Pseudo-rigid body
S	Stand
TLITFP	Tensioned leaf-type isosceles-trapezoidal flexural pivot
VCM	Virtual-center of motion

Variables

a_1, a_2	*X*-coordinate of the end points *B* and *C* of link *BC*
b	Width of the leaf
$\overline{CC'}$, $\overline{DD'}$	Displacements of points *C* and *D*, respectively
E	Elastic modulus
I, I_i	Moments of inertia of the leaf and LITFP *i*, respectively
F	Force
F_{Cx}, F_{Cy}	Component forces at point *C* on the *X*- and *Y*-axis, respectively
F_{Dx}, F_{Dy}	Component forces at point *D* on the *X*- and *Y*-axis, respectively
F_{NC}, $F_{\mathrm{N}D}$	Axial forces applied to link *DC* on points *C* and *D*, respectively
F_{RC}, $F_{\mathrm{R}D}$	Radial forces exerted by link *BC* and *AD* on points *C* and *D* of link *DC*, respectively
h_{f}	Height of the lower plane of LITFP from the ICR
$h_{\mathrm{f}i}$	Height of the lower plane of LITFP *i* from the ICR, *i* = 1, 2
H	Height of the upper plane of LITFP from the ICR
H_i	Height of the upper plane of LITFP *i* from the ICR, *i* = 1, 2
K	Bending stiffness of LITFP
K_{BC}, K_{AD}	Bending stiffness of links *BC* and *AD*, respectively
K_{d}	Bending stiffness of the D-LITFP
K_i	Bending stiffness of the LITFP *i*, *i* = 1, 2
K_{V}	Bending stiffness of the VCM mechanism
$l_{\mathrm{joint}}(i)$	Driving cable length in single joint
l_{r}	Length of the rigid links *A′D* and *B′C*
$l_{\mathrm{segment}}(i)$	Driving cable length in a single segment
$l_{\mathrm{single}}(i)$	Driving cable length in half joint
$l_{\mathrm{total}}(i)$	Driving cable length of the whole continuum robot
M	A pure bending moment
$M_{\max}$	Maximum bending moment which LITFP can bear
n	Position coefficient of ICR
n_i	Position coefficient of the ICR of the LITFP *i*
r	Radius of the circle where the driving cable is located
r_{f}	Result of FEA
r_{p}	Calculation result of the PRB model
R	Bending radius
R_{bend}	Bending radius of the segment
$\boldsymbol{R}_Y$	Rotation matrix around the *Y*-axis
$\boldsymbol{R}_Z$	Rotation matrix around the *Z*-axis
${}^{4}_{0}\boldsymbol{R}$, ${}^{4}_{0}\boldsymbol{P}$	Rotation matrix and displacement vector from $\{O_4\}$ to $\{O_0\}$, respectively
S_{y}	Tensile yield strength
t	Thickness of the leaf
t_i	Thickness of the leaf of LITFP *i*
$\boldsymbol{T}_{\mathrm{segment}}$	Pose transformation matrix of the single segment
$\boldsymbol{T}_{\mathrm{total}}$	End pose transformation matrix of the whole continuum robot
${}^{1}_{0}\boldsymbol{T}$	Coordinate transformation matrix from $\{O_1\}$ to $\{O_0\}$
${}^{2}_{0}\boldsymbol{T}$	Coordinate transformation matrix from $\{O_2\}$ to $\{O_0\}$

${}_1^2\boldsymbol{T}$	Coordinate transformation matrix from $\{O_2\}$ to $\{O_1\}$
α_1, α_2	Bending angles of link BC and AD under the action of bending moment M
$\sigma_{1\max}$, $\sigma_{2\max}$	Maximum stress values corresponding to rotation angles of LITFPs 1 and 2, respectively
$\sigma_{\mathrm{d}\max}$, $\sigma_{\max}$	Maximum stress of the D-LITFP and LITFP, respectively
φ	Bending angle of the half joint
φ_i	Half of the angle between the two leaves of the LITFP i, $i = 1, 2$
φ_X, φ_Y	X- and Y-axis tilt angles, respectively
θ	Rotation angle (stroke) of the VCM mechanism
θ_{d}	Rotation angle of the whole D-LITFP
$\theta_{\mathrm{d}\max}$	Maximum bending angle of the whole D-LITFP
θ_i, $\theta_{i\max}$	(Maximum) Bending angle of the LITFP i, $i = 1, 2$
θ_{joint}, $\theta_{\mathrm{segment}}$	Bending angles of the single joint and single segment, respectively
$\theta_{\max}$	Maximum bending angle of the LITFP
η	Bending direction
η_{joint}, η_{segment}	Bending directions of the single joint and single segment, respectively
ε	Relative error of PRB model with respect to FEA
Δl	Displacement of the force sensor
$\Delta l(i)$	Cable length difference
$\Delta l_{\mathrm{joint}}(i)$	Difference in driving cable length in a single joint
$\Delta l_{\mathrm{segment}}(i)$	Difference in driving cable length in a single segment
$\Delta l_{\mathrm{single}}(i)$	Difference in driving cable length in half joint
$\Delta l_{\mathrm{total}}(i)$	Difference in driving cable length of the whole continuum robot

Acknowledgements This work was supported in part by the National Natural Science Foundation of China (Grant No. U1813221) and the National Key R&D Program of China (Grant No. 2019YFB1311200).

References

1. Qi F, Chen B, Gao S Y, She S G. Dynamic model and control for a cable-driven continuum manipulator used for minimally invasive surgery. The International Journal of Medical Robotics and Computer Assisted Surgery, 2021, 17(3): e2234
2. Omisore O M, Han S P, Xiong J, Li H, Li Z, Wang L. A review on flexible robotic systems for minimally invasive surgery. IEEE Transactions on Systems, Man, and Cybernetics: Systems, 2022, 52(1): 631–644
3. Thomas T L, Kalpathy Venkiteswaran V, Ananthasuresh G K, Misra S. Surgical applications of compliant mechanisms: a review. Journal of Mechanisms and Robotics, 2021, 13(2): 020801
4. Axinte D, Dong X, Palmer D, Rushworth A, Guzman S C, Olarra A, Arizaga I, Gomez-Acedo E, Txoperena K, Pfeiffer K, Messmer F, Gruhler M, Kell J. MiRoR-miniaturized robotic systems for holistic *in-situ* repair and maintenance works in restrained and hazardous environments. IEEE/ASME Transactions on Mechatronics, 2018, 23(2): 978–981
5. Dong X, Axinte D, Palmer D, Cobos S, Raffles M, Rabani A, Kell J. Development of a slender continuum robotic system for on-wing inspection/repair of gas turbine engines. Robotics and Computer-Integrated Manufacturing, 2017, 44: 218–229
6. Buckingham R, Graham A. Nuclear snake-arm robots. Industrial Robot, 2012, 39(1): 6–11
7. Buckingham R, Graham A. Snaking around in a nuclear jungle. Industrial Robot, 2005, 32(2): 120–127
8. Nahar D, Yanik P M, Walker I D. Robot tendrils: long, thin continuum robots for inspection in space operations. In: Proceedings of 2017 IEEE Aerospace Conference. Big Sky: IEEE, 2017, 1–8
9. Liljebäck P, Mills R. Eelume: a flexible and subsea resident IMR vehicle. In: Proceedings of Oceans 2017-Aberdeen Conference. Aberdeen: IEEE, 2017, 1–4
10. Yamauchi Y, Ambe Y, Nagano H, Konyo M, Bando Y, Ito E, Arnold S, Yamazaki K, Itoyama K, Okatani T, Okuno H G, and Tadokoro S. Development of a continuum robot enhanced with distributed sensors for search and rescue. Robomech Journal, 2022, 9(1): 8
11. Russo M, Sriratanasak N, Ba W M, Dong X, Mohammad A, Axinte D. Cooperative continuum robots: enhancing individual continuum arms by reconfiguring into a parallel manipulator. IEEE Robotics and Automation Letters, 2022, 7(2): 1558–1565
12. Wang M F, Dong X, Ba W M, Mohammad A, Axinte D, Norton A. Design, modelling and validation of a novel extra slender continuum robot for *in-situ* inspection and repair in aeroengine. Robotics and Computer-Integrated Manufacturing, 2021, 67: 102054
13. Deashapriya K P, Sampath P A G, Wijekoon W M S B, Jayaweera N D, Kulasekera A L. Biomimetic flexible robot arm design and kinematic analysis of a novel flexible robot arm. In: Proceedings of 2016 Moratuwa Engineering Research Conference (MERCon). Moratuwa: IEEE, 2016, 385–390
14. Li Z, Du R X. Design and analysis of a bio-inspired wire-driven multi-section flexible robot. International Journal of Advanced Robotic Systems, 2013, 10(4): 209
15. Buckingham R, Chitrakaran V, Conkie R, Ferguson G, Graham A, Lazell A, Lichon M, Parry N, Pollard F, Kayani A, Redman M, Summers M, Green B. Snake-Arm Robots: A New Approach to Aircraft Assembly. SAE International 2007-01-3870, 2007,
16. Guardiani P, Ludovico D, Pistone A, Abidi H, Zaplana I, Lee J, Caldwell D G, Canali C. Design and analysis of a fully actuated cable-driven joint for hyper-redundant robots with optimal cable routing. Journal of Mechanisms and Robotics, 2022, 14(2): 021006
17. Bamoriya S, Kumar C S. Kinematics of three segment continuum robot for surgical application. In: Kumar R, Chauhan V S, Talha M, Pathak H, eds. Machines, Mechanism and Robotics. Singapore: Springer, 2022, 1011–1021
18. Kim Y, Cheng S S, Diakite M, Gullapalli R P, Simard J M, Desai J P. Toward the development of a flexible mesoscale MRI-compatible neurosurgical continuum robot. IEEE Transactions on Robotics, 2017, 33(6): 1386–1397
19. De Volder M, Moers A J M, Reynaerts D. Fabrication and control

of miniature McKibben actuators. Sensors and Actuators A: Physical, 2011, 166(1): 111–116

20. Böttcher G, Lilge S, Burgner-Kahrs J. Design of a reconfigurable parallel continuum robot with tendon-actuated kinematic chains. IEEE Robotics and Automation Letters, 2021, 6(2): 1272–1279
21. Yang C H, Geng S N, Walker I, Branson D T, Liu J G, Dai J S, Kang R J. Geometric constraint-based modeling and analysis of a novel continuum robot with shape memory alloy initiated variable stiffness. The International Journal of Robotics Research, 2020, 39(14): 1620–1634
22. Chitalia Y, Jeong S, Yamamoto K K, Chern J J, Desai J P. Modeling and control of a 2-DoF meso-scale continuum robotic tool for pediatric neurosurgery. IEEE Transactions on Robotics, 2021, 37(2): 520–531
23. Park S, Kim J, Kim C, Cho K J, Noh G. Design optimization of asymmetric patterns for variable stiffness of continuum tubular robots. IEEE Transactions on Industrial Electronics, 2022, 69(8): 8190–8200
24. Oliver-Butler K, Childs J A, Daniel A, Rucker D C. Concentric push-pull robots: planar modeling and design. IEEE Transactions on Robotics, 2022, 38(2): 1186–1200
25. Girerd C, Morimoto T K. Design and control of a hand-held concentric tube robot for minimally invasive surgery. IEEE Transactions on Robotics, 2021, 37(4): 1022–1038
26. Rucker C, Childs J, Molaei P, Gilbert H B. Transverse anisotropy stabilizes concentric tube robots. IEEE Robotics and Automation Letters, 2022, 7(2): 2407–2414
27. Lee K, Wang Y Z, Zheng C Q. Twister hand: underactuated robotic gripper inspired by origami twisted tower. IEEE Transactions on Robotics, 2020, 36(2): 488–500
28. Santoso J, Onal C D. An origami continuum robot capable of precise motion through torsionally stiff body and smooth inverse kinematics. Soft Robotics, 2021, 8(4): 371–386
29. Wu S, Ze Q J, Dai J Z, Udipi N, Paulino G H, Zhao R K. Stretchable origami robotic arm with omnidirectional bending and twisting. Proceedings of the National Academy of Sciences of the United States of America, 2021, 118(36): e2110023118
30. Kang B, Kojcev R, Sinibaldi E. The first interlaced continuum robot, devised to intrinsically follow the leader. PLoS One, 2016, 11(2): e0150278
31. Hawkes E W, Blumenschein L H, Greer J D, Okamura A M. A soft robot that navigates its environment through growth. Science Robotics, 2017, 2(8): eaan3028
32. Sadeghi A, Del Dottore E, Mondini A, Mazzolai B. Passive morphological adaptation for obstacle avoidance in a self-growing robot produced by additive manufacturing. Soft Robotics, 2020, 7(1): 85–94
33. Awtar S, Slocum A H. Constraint-based design of parallel kinematic *XY* flexure mechanisms. Journal of Mechanical Design, 2007, 129(8): 816–830
34. Howell L L, Midha A. A method for the design of compliant mechanisms with small-length flexural pivots. Journal of Mechanical Design, 1994, 116(1): 280–290
35. Ping Z Y, Zhang T C, Gong L, Zhang C, Zuo S Y. Miniature flexible instrument with fibre bragg grating-based triaxial force sensing for intraoperative gastric endomicroscopy. Annals of Biomedical Engineering, 2021, 49(9): 2323–2336
36. Wei X Y, Zhang Y X, Ju F, Guo H, Chen B, Wu H T. Design and analysis of a continuum robot for transnasal skull base surgery. The International Journal of Medical Robotics and Computer Assisted Surgery, 2021, 17(6): e2328
37. Wang H D, Wang X L, Yang W L, Du Z J. Design and kinematic modeling of a notch continuum manipulator for laryngeal surgery. International Journal of Control, Automation, and Systems, 2020, 18(11): 2966–2973
38. Kato T, Okumura I, Kose H, Takagi K, Hata N. Tendon-driven continuum robot for neuroendoscopy: validation of extended kinematic mapping for hysteresis operation. International Journal of Computer Assisted Radiology and Surgery, 2016, 11(4): 589–602
39. Tian J W, Wang T M, Fang X, Shi Z Y. Design, fabrication and modeling analysis of a spiral support structure with superelastic Ni-Ti shape memory alloy for continuum robot. Smart Materials and Structures, 2020, 29(4): 045007
40. Pei X, Yu J J, Zong G H, Bi S S. An effective pseudo-rigid-body method for beam-based compliant mechanisms. Precision Engineering, 2010, 34(3): 634–639